Structure, dynamics and roX2-lncRNA binding of tandem double-stranded RNA binding domains dsRBD1,2 of *Drosophila* helicase Maleless

Supplementary material

rox2-SL3.fw	TTACATATAGCTTTAGAGATCGTTTCG
rox2-SL3.rv	GCTTGATTTTGCTTCGGAGA
rox2-SL7.fw	GACGTGTAAAATGTTGCAAATTAAG
rox2-SL7.rv	TGACTGGTTAAGGCGCGTA
7SK.fw	GATAACCCGTCGTCATCCAG
7SK.rv	AGTAATTCTGCCTGGCGTTG

Table S1. Different primers for qPCR used in this study.

Supplementary figures.

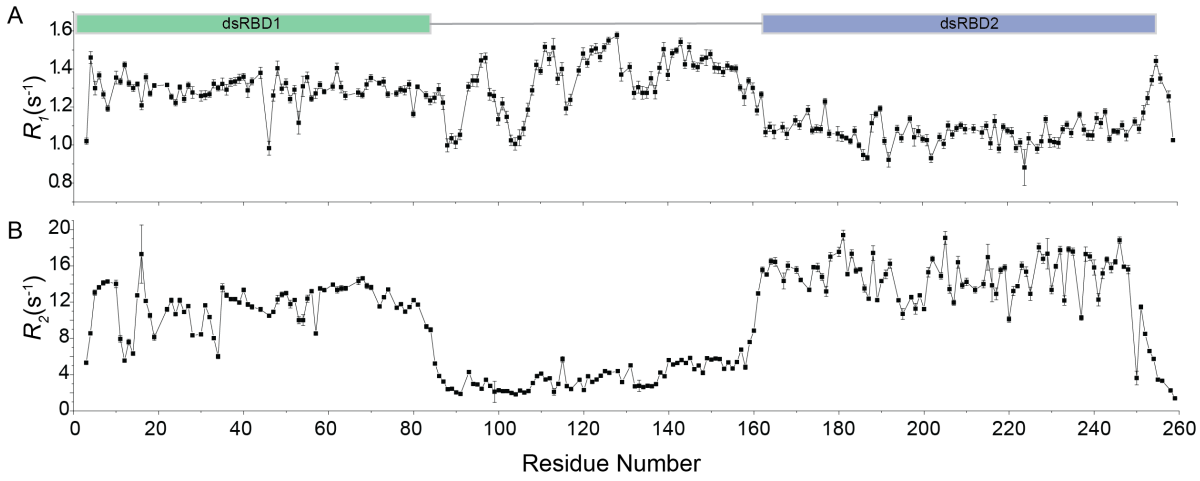

Figure S1: (A) & (B) ^{15}N transverse relaxation analysis of dsRBD1,2 in the free form suggesting that the two domains tumble independently in solution.

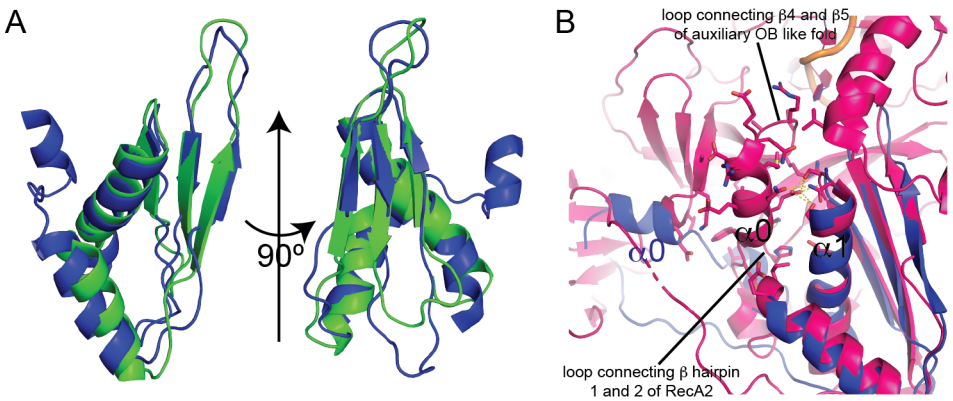

Figure S2: (A) Comparison of dsRBD1 (green) and dsRBD2 (blue) NMR structures. The two domains superpose well with an RMSD of 1.2 Å. dsRBD2 contains an extra α0 helix in the structure. (B) Superposition of dsRBD2 structures as determined by NMR (blue) and

crystallography (magenta) (in the MLE_{core} domain, PDB ID: 5AOR) showing the packaging of $\alpha 0$ helix in the crystal structure. The $\alpha 0$ helix in the NMR structure is flexible.

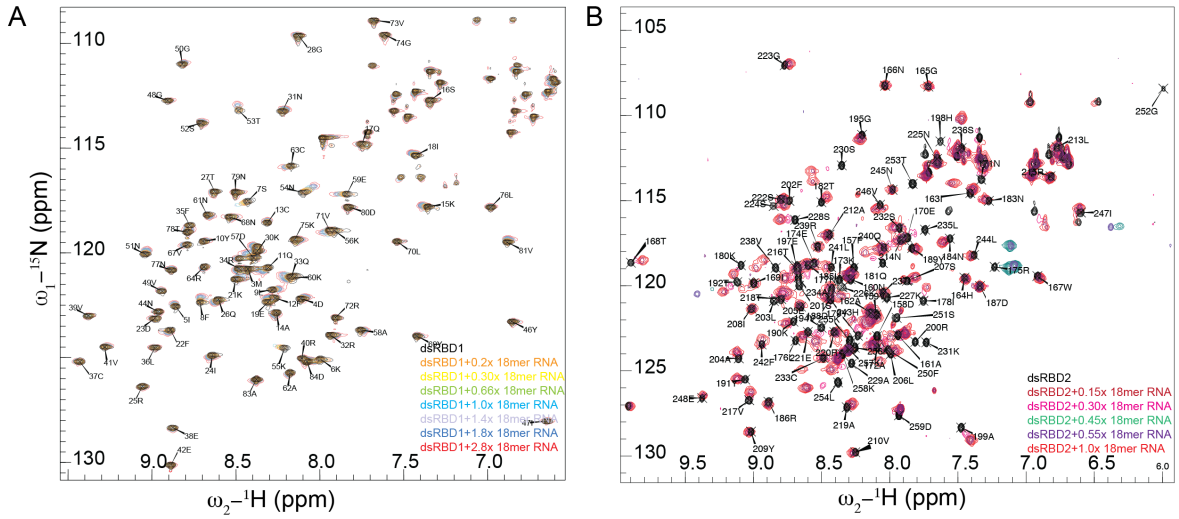

Figure S3: ^{1}H, ^{15}N HSQC NMR titration of individual dsRBD domains with $SL7^{18mer}$ dsRNA.

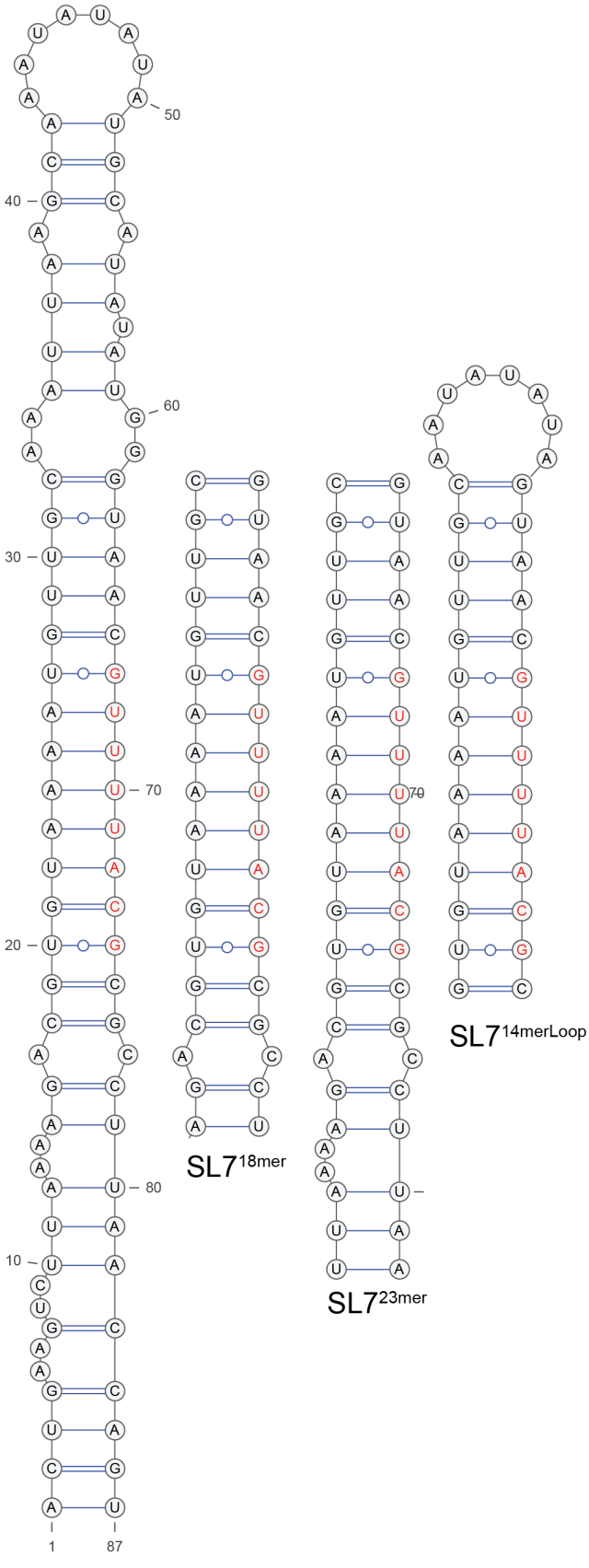
SL7
SL7^18mer
SL7^23mer
SL7^14merLoop

Figure S4: Different RNA's used in this study and derived from roX2 SL7 stem are shown. The roX-box region is indicated using red fonts.

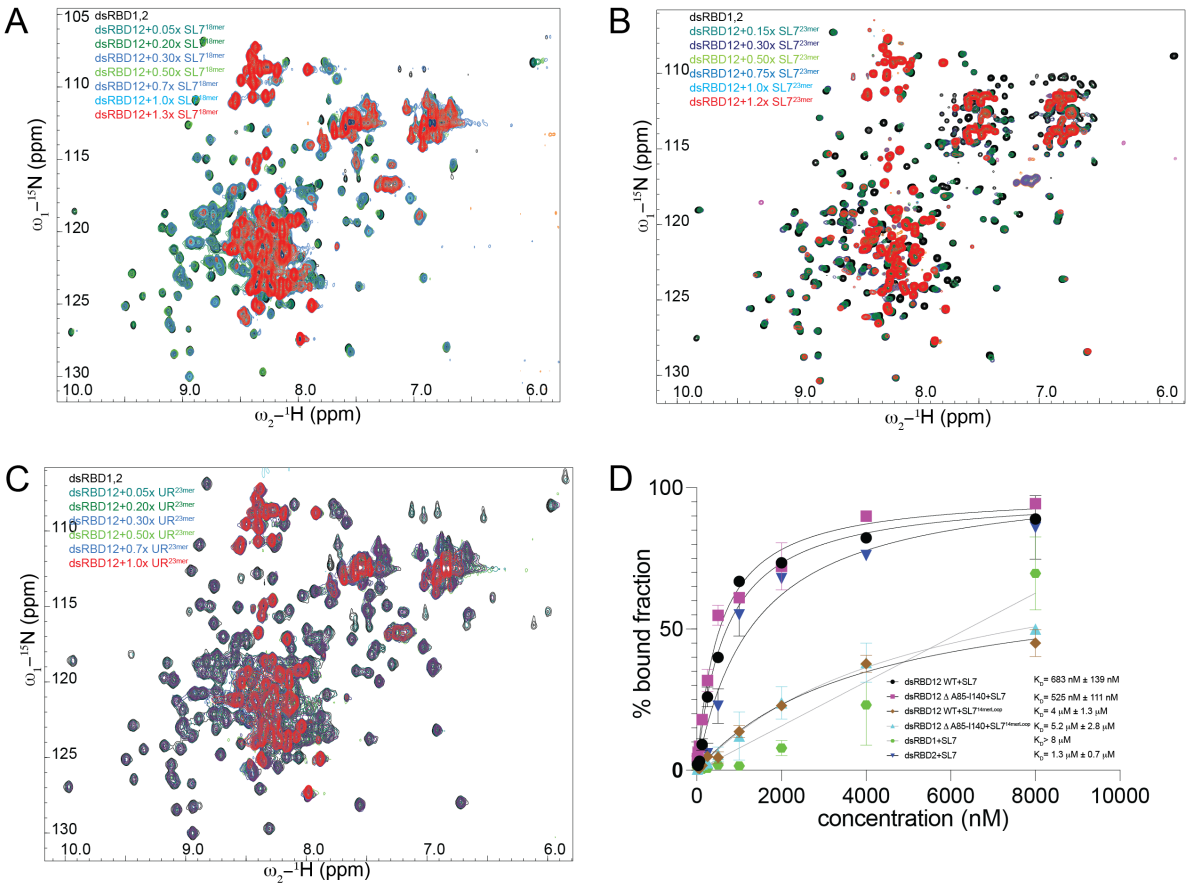

Figure S5: Full ^{1}H, ^{15}N HSQC NMR titration of dsRBD1,2 with (A) $SL7^{18mer}$, (B) $SL7^{23mer}$ and (C) UR^{23mer}. All titrations show severe line broadening with increasing concentration of RNA except in the linker region. (D) Filter binding experiments of dsRBD1,2, dsRBD1, dsRBD2 and dsRBD1,2 (Δ A85-I140) with SL7 and $SL7^{14merLoop}$ dsRNA. Error bars represent standard deviation of two replicates.

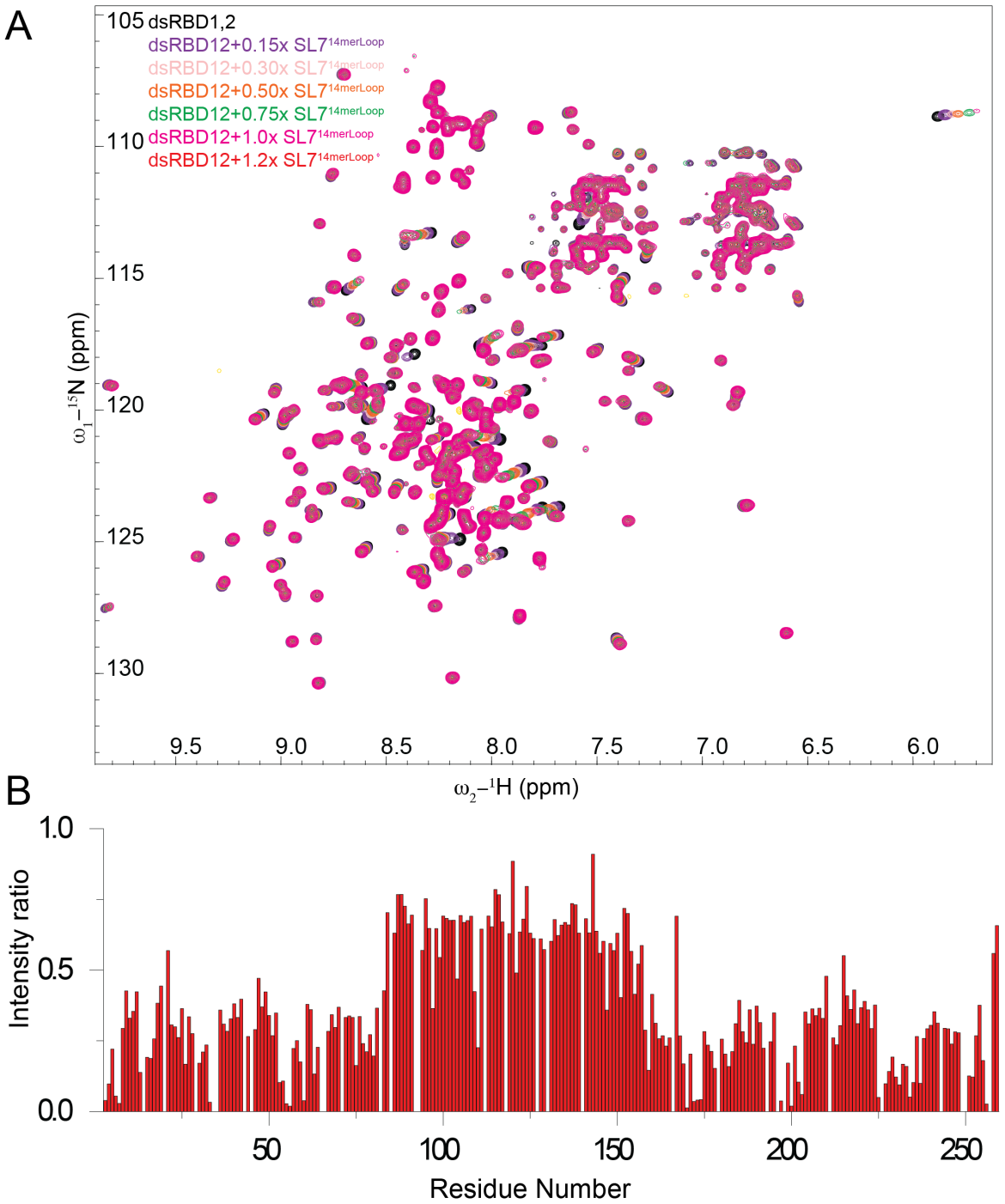

Figure S6: (A) ^{1}H, ^{15}N HSQC NMR titration of dsRBD1,2 with $SL^{14merLoop}$. (B) Intensity ratios of dsRBD1,2 + $SL^{14merLoop}$ and dsRBD1,2 free showing a minor drop of intensity within the linker region and signifying its flexibility.

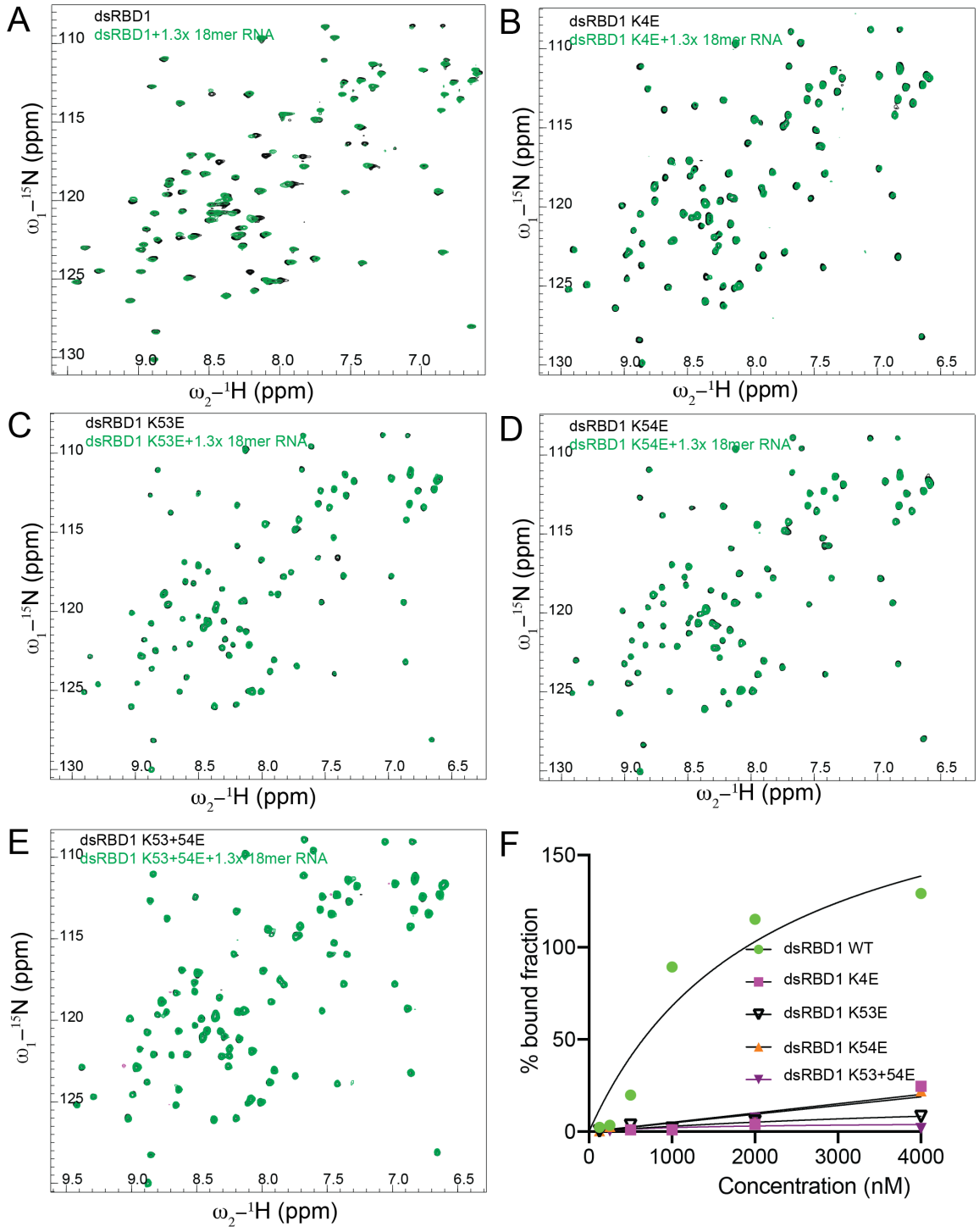

Figure S7: RNA binding of dsRBD1 mutants (A) dsRBD1, (B) dsRBD1 K4E, (C) dsRBD1 K53E, (D) dsRBD1 K54E and (E) dsRBD1 K53+54E upon titration with 1.3x $SL7^{18mer}$ RNA. (F) Filter binding experiments of individual dsRBD1 RNA binding mutants for SL7 binding. Only dsRBD1 WT shows binding with a K_D of 2 µM ± 0.4 µM. The assay was performed in no salt buffer to detect the binding of dsRBD1 properly in filter binding assays.

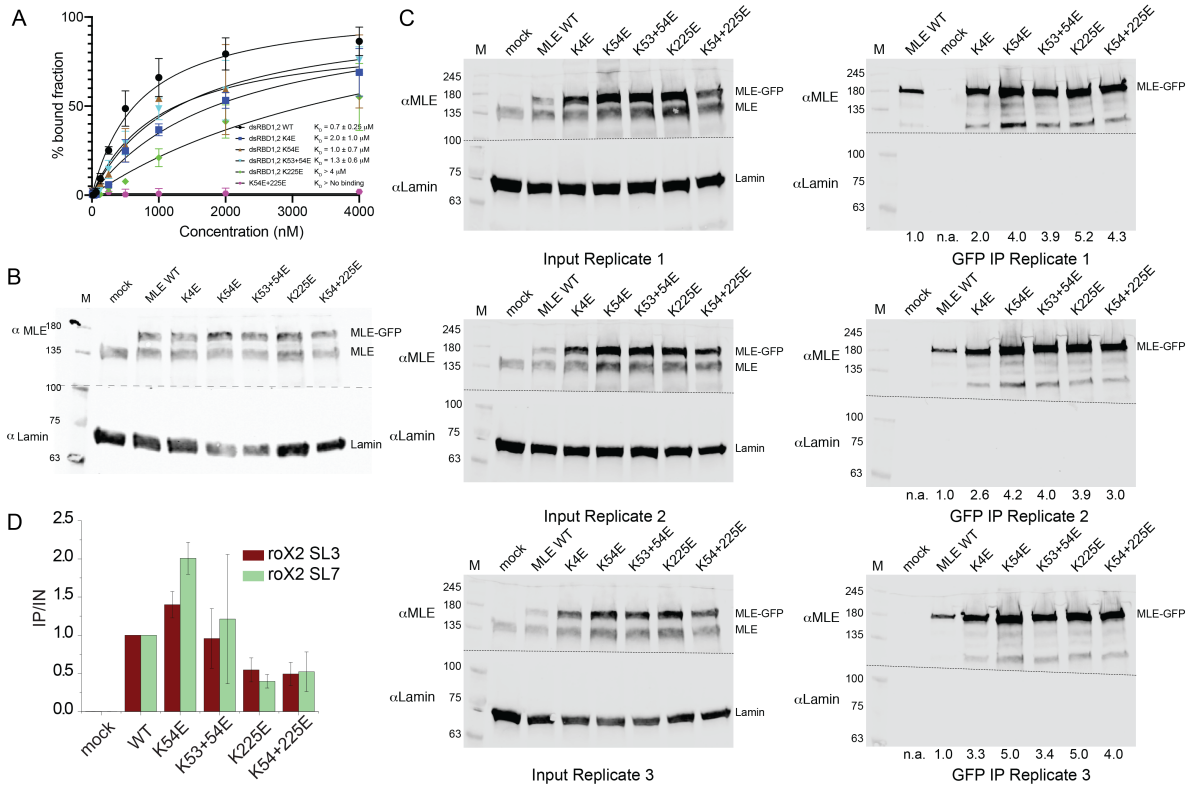

Figure S8: (A) Effect of dsRBD1 RNA binding mutations in the dsRBD1,2 context as determined by filter binding experiments. SL7 RNA was used for these experiments. The error bars represent standard deviation of two replicates (B) Western blot analysis of S2 cell lines stably expressing MLE-GFP and its dsRBD1,2 variants used for immunostaining studies. Anti-MLE antibody was used to detect endogenous MLE and MLE-GFP variants, respectively. Lamin served as loading control. (C) Western blot analysis of S2 cell lines stably expressing MLE-GFP and its dsRBD1,2 variants, which were used for three independent replicates of *in vivo* RNA immunoprecipitation experiments shown in (D). MLE-GFP levels in input (left) and GFP-immunoprecipitated fractions (right) were detected using anti-MLE antibody. Lamin served as loading control. The fraction of each immunoprecipitated MLE-GFP variant relative to MLE-GFP wild type is given. (D) *In vivo* RIP of MLE-GFP wild type or mutated in dsRBD1,2. Enrichment of roX2 by the MLE-GFP derivatives is shown relative to MLE-GFP wild type. Error bars represent average standard deviations for three independent biological replicates.